GREEN TECHNOLOGY & INNOVATION
Volume 2 (2026) · ISSN 2979-1456

TECHNICAL ARTICLE

An Energy-Data-Anchored Probabilistic Digital-Twin Framework for Coupled Structural–Envelope Degradation and Local Energy-Demand Amplification in Low-Carbon Buildings

Seyed Reza Samaei[1*], Assed Naked Haddad[2], James Riffat[1]

[1] World Society of Sustainable Energy Technologies, Nottingham, United Kingdom
[2] Environmental Engineering Program, Escola Politécnica, Universidade Federal do Rio de Janeiro (UFRJ), Rio de Janeiro, Brazil

RECEIVED 1 August 2026 · REVISED 25 August 2026 · ACCEPTED 21 September 2026 · PUBLISHED 14 October 2026

ABSTRACT

Long-horizon building-performance models commonly treat operational energy use and physical deterioration as independent processes, despite the potential for envelope degradation to increase thermal demand and for sustained HVAC operation to alter thermal–moisture exposure. This study develops an energy-data-anchored probabilistic digital-twin framework that integrates three coupled lifecycle states: structural/support-condition loss, envelope thermal and leakage loss, and thermal-load memory. A Coupled Structural–Energy Instability Index (CSEI), defined as the spectral abscissa of the frozen local Jacobian, is introduced as a deliberately bounded local modal-transition diagnostic. An autoregressive grey-box observation model was calibrated using 2016 hourly electricity data and independently evaluated one step ahead against the complete 2017 record of a 12,365.4 m^2 office building, achieving R^2 = 0.933, CV(RMSE) = 6.65%, and NMBE = 0.029%. Within a 25-year, 12,000 m^2 reference scenario, bidirectional coupling increased lifecycle electricity consumption and operational carbon emissions by 16.7% and 15.8%, respectively, relative to the energy-decoupled configuration. On the monthly evaluation grid, CSEI first became non-negative at 17.58 years. Across 5,000 parameter–climate realisations, mean lifecycle electricity consumption and carbon emissions were 32.091 GWh and 11.552 $ktCO_2e$, respectively; 98.36% of trajectories crossed the CSEI transition boundary by year 25, with a conditional median onset of 17.67 years. In 100 correctly specified synthetic recovery experiments, median state RMSEs were 0.00205, 0.00121, and 0.00785, and the median absolute onset-reconstruction error was 0.56 years. Collectively, the results provide empirical validation of the energy-observation layer and demonstrate numerical, probabilistic, and inference consistency of the coupled framework. The reported lifecycle trajectories and CSEI onset times remain conditional reference-scenario outputs and should not be interpreted as field-validated deterioration predictions or structural-safety criteria.

KEYWORDS Probabilistic digital twin, Building degradation, Energy demand, Bayesian updating, CSEI, Low-carbon buildings

1. Introduction

The operating carbon of a building is not fixed at commissioning. Envelope joints loosen, seals fail, insulation becomes discontinuous, HVAC efficiency changes and repeated thermal or moisture exposure alters the condition of structural and non-structural components. Yet many lifecycle models hold envelope properties constant while structural assessment proceeds in a separate model. That separation is convenient, but it removes a physically plausible route by which deterioration increases thermal demand and prolonged system operation modifies the exposure that drives further deterioration.

* Corresponding author. Email address: seyedreza.samaei1984@gmail.com (Seyed Reza Samaei)

© 2026 The Author(s).
Published by Caravel Press.

doi.org/10.65582/gti.2026.018

Digital twins offer a useful architecture for closing that gap because they combine a state model, observations, inference and decisions rather than treating simulation as a one-off exercise (Madni *et al.* 2019; Rasheed *et al.* 2020; Wright and Davidson 2020). Construction and building research has moved from static building information models toward connected representations that can assimilate measured performance and support predictive action (Boje *et al.* 2020; Deng *et al.* 2021). Probabilistic graphical formulations further show how uncertainty, data assimilation and control can be placed within a coherent digital-twin structure (Kapteyn *et al.* 2021).

Recent building digital-twin research has moved beyond static asset representation toward hybrid simulation–data models and continuously updated building-energy management systems. Hybrid digital twins have used operational data to correct physics-based building simulations, while digital-twin-enabled energy management systems have demonstrated the value of integrated information fusion for operational prediction and control. In parallel, structural digital-twin research has advanced Bayesian model updating through learnable mappings and multi-fidelity state estimation. These studies strengthen domain-specific prediction and calibration, but they do not provide a long-horizon criterion for detecting local modal amplification within a coupled structural–envelope–energy deterioration process (Oh *et al.* 2024; Hwang *et al.* 2025; Torzoni *et al.* 2025). Recent studies have also begun to quantify how ageing and degradation of envelope components alter operational energy demand. Reported pathways include deterioration of insulation, insulated glazing, airtightness, solar reflectivity and other thermal properties that are commonly treated as fixed at commissioning (Taki and Zakharanka 2023). Recent structural-health-monitoring digital-twin research likewise emphasises that field deployment requires explicit treatment of sensor limitations, model updating, uncertainty and model-form discrepancy rather than reliance on simulation alone (Sun *et al.* 2025; Andrés Arcones *et al.* 2024). This literature supports a coupled lifecycle perspective, but it also demonstrates why an electricity record by itself cannot identify long-term structural or envelope deterioration laws.

Two limitations remain. First, energy calibration alone cannot establish the evolution of a coupled structural–envelope system. Second, a rising damage index or annual energy use does not reveal whether their interaction has crossed from slow deterioration into a self-amplifying regime. The latter requires a dynamical stability measure. The present paper therefore treats instability as a local property of the updated coupled state, not as a visual label attached after a threshold has been exceeded. The mathematical quantity underlying CSEI—the spectral abscissa of a local Jacobian—is established in dynamical-systems analysis. The contribution claimed here is therefore not a new stability theorem. It is the integration of this deliberately limited diagnostic into an energy-anchored, three-state building lifecycle framework, together with explicit coupling isolation, state recovery, uncertainty propagation and finite-time diagnostics that define what the local index can and cannot establish.

Short-horizon stability preservation has previously been examined as an operational-control problem (Samaei and Riffat 2026). That study addressed supervisory action selection over a short operational horizon. The present study does not reuse that control formulation. It introduces different lifecycle states, a 25-year monthly degradation horizon, an empirical electricity-observation anchor, parameter–climate uncertainty propagation, controlled state-recovery experiments and a frozen-time modal diagnostic. No rolling-horizon optimisation, intervention policy, renewable-storage design or self-healing control is evaluated in the present paper.

The investigation addresses four research questions and associated expectations:

RQ1/H1: How do otherwise identical energy-decoupled, one-way and bidirectional formulations differ in lifecycle electricity, carbon and deterioration? It is expected that retaining both feedback directions will increase these outputs relative to the energy-decoupled formulation.

RQ2/H2: Does the spectral abscissa of the frozen local Jacobian change sign within the 25-year reference horizon, and is its implementation consistent with frozen-eigenmode and finite-time diagnostics? It is expected that the reference trajectory will exhibit a sign change before year 25,

while finite-time analysis will demonstrate the limits of interpreting that sign as a global-stability condition.

RQ3/H3: Does sequential state assimilation and regularised parameter recovery reduce state-tracking error and retrospective onset-reconstruction error relative to a biased prior-only trajectory? It is expected that posterior RMSE and absolute onset-reconstruction error will decrease and that posterior state intervals will achieve approximately nominal coverage in correctly specified synthetic recovery experiments.

RQ4/H4: Which of the nine uncertain state-model parameters govern cumulative instability exposure and restricted time to onset? It is expected that nonlinear deterioration acceleration and the bidirectional operational-feedback pathway will dominate the total-effect indices.

The contribution is an auditable chain from measured hourly electricity to a reduced-order observation model, a three-state coupled lifecycle formulation, sequential state updating, regularised parameter recovery, 5,000-realisation parameter–climate uncertainty propagation, local modal and finite-time diagnostics, and global sensitivity analysis of nine uncertain state-model parameters (Figure 1). Empirical validation is confined to the electricity-observation layer. Coupled-state behaviour is supported through analytical consistency, limiting cases, time-step convergence, correctly specified synthetic recovery experiments and probabilistic numerical verification. All reported numerical analyses use the same locked reference parameter set, state definitions, monthly load profile, uncertainty distributions and disclosed random seeds.

2. Framework and validation design

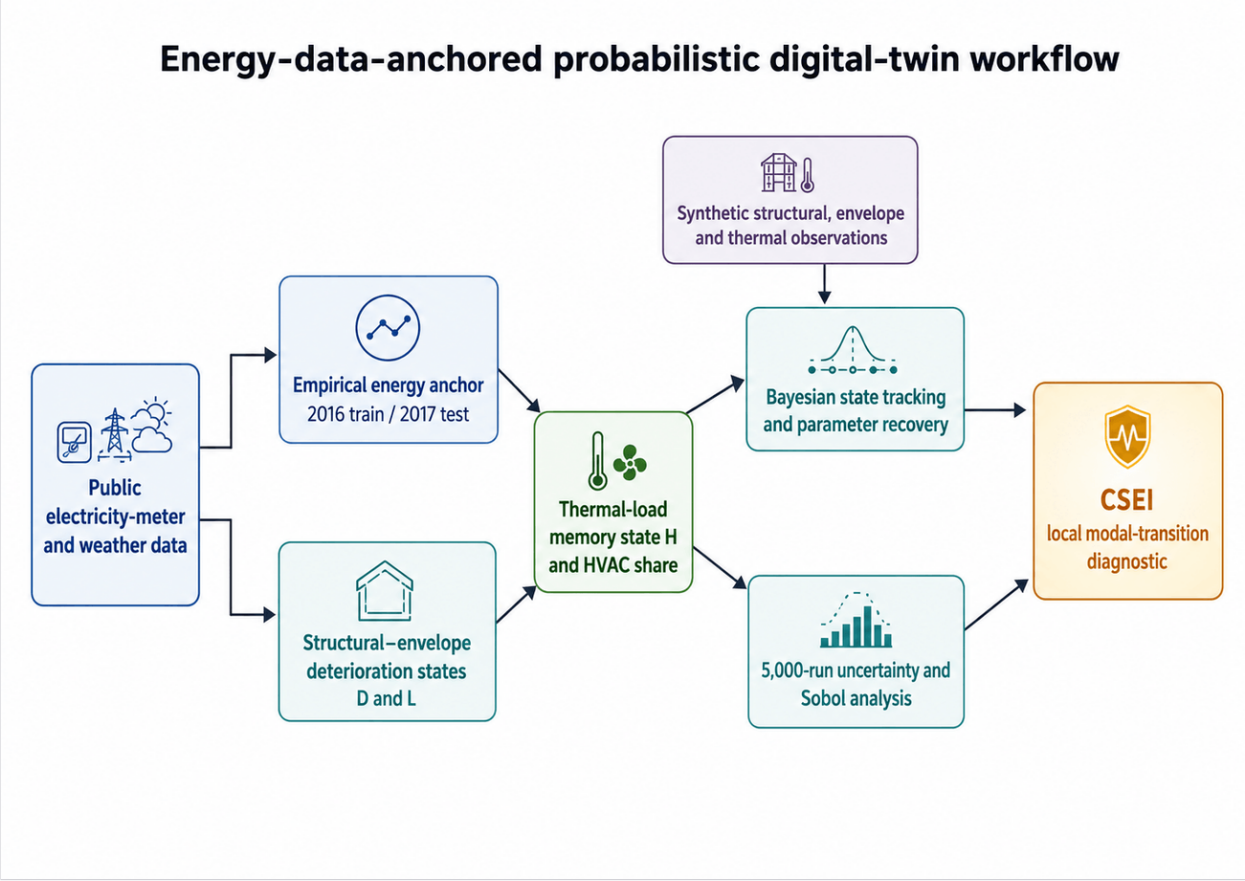

Figure 1. Energy-data-anchored probabilistic digital-twin workflow. Public electricity and weather data support the operational observation layer, whereas structural–envelope recovery is evaluated using controlled synthetic observations. CSEI is an assessment output; no closed-loop intervention is simulated.

2.1. Validation hierarchy

Validation and verification are treated as distinct layers (Table 1). First, the electricity observation model is evaluated on an unseen calendar year, providing empirical out-of-sample evidence for the operational data layer. Second, the coupled state equations are verified through energy-decoupled and one-way limiting cases and through time-step refinement. Third, the CSEI implementation is checked using frozen-eigenmode propagation and is complemented by finite-time singular-value analysis to expose non-normal transient amplification. Fourth, state tracking and parameter recovery are evaluated using quarterly synthetic observations generated from a reference trajectory and repeated over 100 independent recovery experiments. Fifth, uncertainty estimates are examined using 5,000 parameter–climate realisations, Monte Carlo convergence and sampling-error diagnostics. These layers do not constitute field validation of long-term structural deterioration; they establish empirical validity for the energy layer and numerical, statistical and inference consistency for the coupled framework.

Table 1. Validation and verification hierarchy used to distinguish empirical validation, numerical verification and deployment limits.

Evidence layer	Question	Final implementation	Supported claim
Empirical energy validation	Can the observation model reproduce unseen meter behaviour?	2016 fitting; independent 2017 one-step-ahead test; R^2, RMSE, CV(RMSE), NMBE and parity analysis	Energy-observation accuracy
Limiting-case verification	Do coupling pathways behave as mathematically specified?	Energy-decoupled, one-way and bidirectional configurations	Correct pathway isolation
Numerical convergence	Are lifecycle outputs stable to time-step refinement?	RK4 at 1, 2, 4 and 8 substeps per month	Integration stability
CSEI implementation	Does the reported sign match the dominant frozen mode?	Matrix-exponential eigenmode propagation at years 10, 20 and 24	Internal frozen-modal consistency
Finite-time diagnostic	Does frozen-modal decay exclude transient amplification?	Variational singular-value gains over 3-, 6- and 12-month windows	Scope and limitation of CSEI
State and parameter recovery	Can biased priors be corrected?	Quarterly observations; 2,500 particles; 100 recovery experiments	Internal recoverability under correctly specified synthetic tests
Uncertainty convergence	Are ensemble estimates numerically stable?	5,000 lognormal parameter draws; AR(1) climate; convergence and MCSE	Stable probabilistic estimates
External structural field validation	Are long-term coefficients validated for a specific building stock?	Not claimed	Identified deployment requirement

2.2. Empirical energy anchor

The operational anchor uses the Building Data Genome Project 2, an open collection of hourly meter, building-metadata and weather records (Miller *et al.* 2020). The office meter Hog_office_Napoleon was selected because it provides an aligned 17,544-hour record over 2016–2017 and a reported floor area of 12,365.4 m^2. Annual electricity use was 1,140,900.84 kWh in 2016 and 1,123,697.12 kWh in 2017, corresponding to 92.27 and 90.87 kWh m^{-2} $year^{-1}$. Their unrounded two-year mean, 91.5699 kWh m^{-2} $year^{-1}$, anchors the baseline whole-building electricity of the reference scenario.

A ridge-regularised autoregressive grey-box observation model was fitted to the 2016 record. In linear form, the model was

$$\hat{y}_t = \beta_0 + \sum_r \beta_r z_{r,t} + \sum_{l\in\{1,2,24,48,168\}} \varphi_l y_{t-l}, \quad (1)$$

where $z_{r,t}$ contained dry-bulb temperature, squared temperature, dew point, sea-level pressure, wind speed, one sine–cosine pair for the hourly cycle, one pair for the weekly cycle, one pair for the annual cycle, and a weekend indicator. The fitted design therefore contained 17 predictors excluding the intercept: five weather variables, six Fourier terms, one calendar indicator and five autoregressive lags.

Ridge regression used an intercept and the locked case-specific regularisation coefficient α=10. Predictors were retained in their native units; accordingly, α is reported only as an implementation constant for this observation model and is not claimed to be a transferable hyperparameter. The 2017 outcomes were not used for coefficient fitting or regularisation selection.

Missing weather values were linearly interpolated and then forward- and backward-filled. Missing meter values were linearly interpolated and constrained to non-negative values. Meter and weather timestamps were aligned on their common hourly index. Construction of the 168-hour maximum lag removed the first 168 hours of the 2016 record, leaving 8,616 lag-complete training observations. The full 8,760-hour 2017 calendar year was retained for testing because its initial lagged values were available from the preceding record. The test was strictly one step ahead and used observed lagged electricity; it was not a recursively free-running annual forecast (Figure 2).

The performance measures were defined as $RMSE = [n^{-1}\Sigma_t(\hat{y}_t - y_t)^2]^{1/2}$, $CV(RMSE) = 100 \times RMSE/\bar{y}$ and $NMBE = 100 \times \Sigma_t(\hat{y}_t - y_t)/(n\bar{y})$. Figure 3 uses 1,800 test observations sampled without replacement using seed 20260728. After the independent test metrics had been fixed, the 2016 and 2017 observations were pooled only to calculate the descriptive monthly whole-building electricity shares used in the lifecycle scenario. The 2017 outcomes therefore affected the lifecycle load profile but not the fitted observation-model coefficients or the reported out-of-sample metrics.

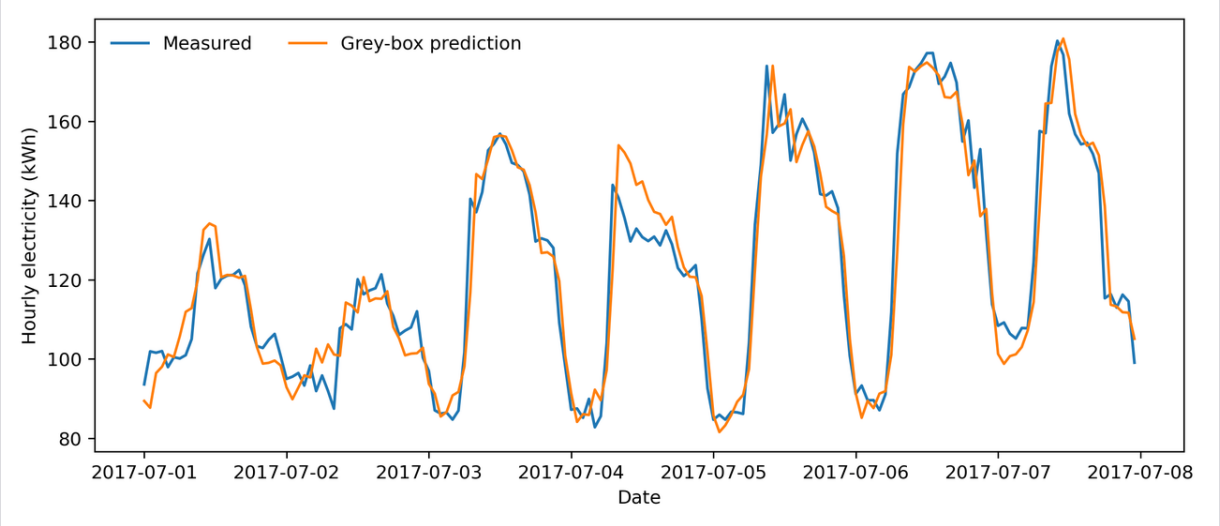

Figure 2. Measured and predicted hourly electricity during an illustrative unseen week in July 2017.

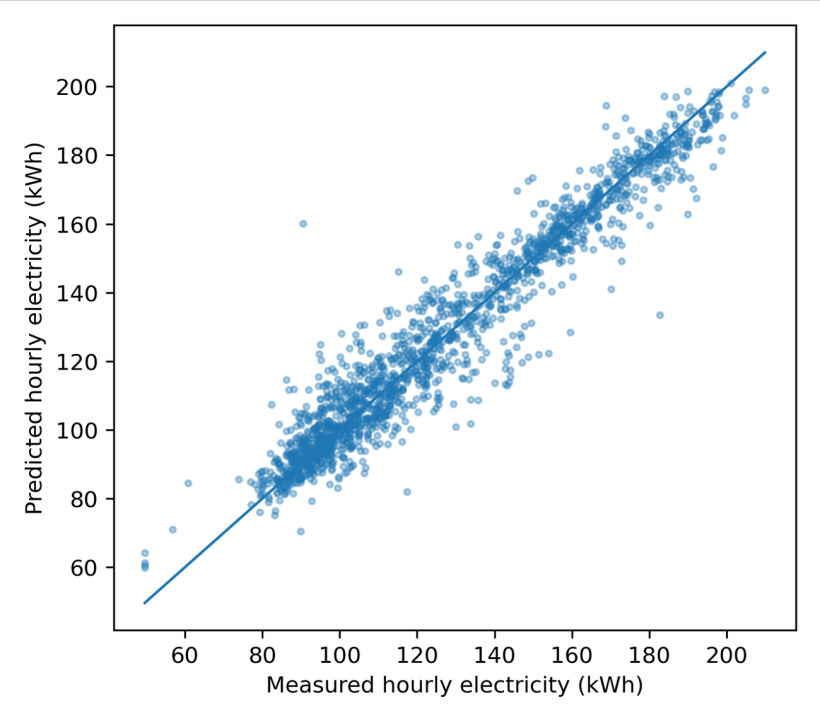

Figure 3. Out-of-sample parity for a reproducible 1,800-point subset of the 2017 test year.

Table 2. Empirical performance of the hourly electricity observation model.

Period	R^2	RMSE (kWh h^{-1})	CV(RMSE) (%)	NMBE (%)
2016 training	0.933	8.88	6.81	0.000
2017 independent test	0.933	8.53	6.65	0.029

The 2017 one-step-ahead CV(RMSE) and NMBE values are below the hourly thresholds commonly used as descriptive calibration references in ASHRAE Guideline 14-2023 (Table 2). This is not presented as formal Guideline 14 compliance because the autoregressive evaluation uses observed lagged electricity and is not a recursively free-running calibrated building simulation. The near-identical training and independent-year R^2 values nevertheless show that the operational anchor is not supported solely by an in-sample fit. The meter does not separate HVAC, lighting and plug loads; the lifecycle model therefore applies a fixed scenario HVAC share of 0.58 to the whole-building baseline rather than treating the meter as a direct HVAC measurement.

3. Coupled lifecycle model

3.1. State definition

The reduced-order state is $x(t) = [D(t), L(t), H(t)]^T$. D is a dimensionless structural/support-condition loss coordinate, whereas L is a separate dimensionless envelope thermal and leakage-loss coordinate. D does not directly represent insulation or airtightness degradation; these effects are represented by L. The coefficient c_D maps structural or support-condition deterioration into envelope loss. H is a dimensionless thermal-load memory state referenced to the initial operating condition and represents sustained HVAC runtime and associated thermal–moisture exposure. Electricity consumption itself is not interpreted as mechanically damaging the structure. All states are evaluated only within the prespecified 25-year analysis domain.

$$\frac{dD}{dt} = k_D(1 - D) + q_D D^3 + c_H s(H - 1)(1 - D) \tag{2}$$

$$\frac{dL}{dt} = k_L(1 - L) + c_D D^2(1 - L) + c_{LH} s(H - 1)(1 - L) \tag{3}$$

$$\frac{dH}{dt} = \frac{C_j\left(1 + u_1 L + u_2 L^2\right)/COP_{rel} - H}{\tau} \tag{4}$$

Here, t is measured in years, and C_j is the month-specific climate multiplier defined in Section 3.2. The nominal relative coefficient of performance was fixed at COP_{rel}=1.0 in all reported analyses. The deterministic reference and limiting-case trajectories used ε_j=0, whereas the stationary AR(1) disturbance was activated only in the parameter–climate uncertainty analysis. The H-to-D and H-to-L terms represent hypothesised exposure-mediated feedback pathways, reflecting the possibility that sustained HVAC operation may coincide with prolonged thermal and moisture exposure. They do not imply that electricity consumption itself causes structural damage. These feedback coefficients are scenario parameters and were not empirically identified from the electricity dataset.

The smooth activation function $s(z) = \ln[1 + \exp(8z)]/8$ is a regularised approximation to the positive-part operator. It remains slightly positive within a narrow transition region around H=1, with $s(0) = ln(2)/8 = 0.08664$. It should therefore be interpreted as a smooth transition-band exposure term rather than an exact zero-to-positive switch. Consequently, the selected formulation introduces a small baseline feedback contribution at H=1, and the reported numerical results are conditional on this activation definition. Equation (2) does not guarantee the global invariance of D≤1 because the nonlinear acceleration term $q_D D^3$ is not multiplied by 1−D. The results are therefore interpreted only within the prescribed 25-year lifecycle state domain. Protective numerical bounds of $0 \le D, L \le 0.99$ and 0.05≤H≤5.0 were imposed solely to prevent solver failure outside the intended domain; no reference or uncertainty trajectory reached these bounds.

3.2. Electricity and carbon mapping

The reference scenario represents a 12,000 m^2, ten-storey office building. Its initial annual whole-building electricity is E_0=1,098,838.8 kWh $year^{-1}$, obtained from the locked mean EUI of 91.5699 kWh m^{-2} $year^{-1}$. The twelve empirical monthly shares reported in Table A1 are repeated in each lifecycle year. The HVAC share f_{HVAC}=0.58, initial grid factor 0.42 $kgCO_2e$ kWh^{-1} and annual grid-factor decline of 1.2% are explicit scenario assumptions rather than estimates for a named electricity system.

Let $j \in \{0, \ldots, 299\}$ denote lifecycle month and let q(j)=j mod 12 denote the calendar-month index, with q=0 corresponding to January. The monthly climate multiplier is

$$C_j = 1 + 0.15 \sin\left[2\pi q(j)/12\right] + \varepsilon_j \tag{5}$$

Baseline and degradation-adjusted whole-building electricity in month j are

$$E_{0,j} = E_0\, w_q(j), \qquad \sum_{q=0}^{11} w_q = 1, \tag{6}$$

$$E_j = E_{0,j}\left[(1 - f_{HVAC}) + f_{HVAC} H_j\right] \tag{7}$$

The grid emission factor is

$$EF_j = 0.42(1 - 0.012)^{j/12}\ kgCO_2e\ kWh^{-1} \tag{8}$$

Lifecycle electricity and operational carbon are

$$ELC = 10^{-6}\sum_{j=0}^{299} E_j\ GWh \tag{9}$$

$$CLC = 10^{-6}\sum_{j=0}^{299} E_j\, EF_j\ ktCO_2e \tag{10}$$

Here H_j is the updated monthly state value used in the locked implementation. The factor 10^{-6} converts kWh to GWh in Equation (9) and $kgCO_2e$ to $ktCO_2e$ in Equation (10). The disturbance ε_j evolves continuously across December–January boundaries and is not reset at the beginning of each lifecycle year.

3.3. Coupled Structural–Energy Instability Index

At each lifecycle month, the local Jacobian $J=\partial f/\partial x$ is evaluated at the updated state while the exogenous climate term is fixed at its annualised reference value C_J=1.0. The Coupled Structural–Energy Instability Index is the spectral abscissa of this frozen Jacobian:

$$CSEI(t) = \max_i\ \mathrm{Re}\{\lambda_i\left[J(x(t),\ t)\right]\} \tag{11}$$

CSEI<0 indicates asymptotic decay of the dominant frozen eigenmode, CSEI=0 denotes a frozen-modal transition boundary, and CSEI>0 indicates local frozen-modal amplification. Because the lifecycle system is nonlinear, non-autonomous and potentially non-normal, the sign of CSEI is not a sufficient condition for global nonlinear stability, absence of finite-time transient amplification, structural collapse, serviceability failure or code compliance. CSEI is therefore interpreted only as a local frozen-time modal-transition diagnostic. In practical terms, CSEI answers a local modal question—whether the locally linearised coupled state tends to decay or amplify at a given month—whereas the finite-time diagnostic examines whether perturbations can still grow over a finite interval even when the local modal indicator remains negative.

The nominal onset time was defined on the locked monthly evaluation grid as

$$T\times = \min\{j/12 : CSEI_j \geq 0\} \tag{12}$$

For trajectories that did not cross by year 25, T× was treated as right-censored and assigned infinity for the purpose of defining the restricted onset output

$$T_R = \min(T\times,\ 25) \tag{13}$$

Cumulative instability exposure was defined as

$$J_{inst} = \int_0^{25} \max\left[CSEI(t),\ 0\right] dt \tag{14}$$

which is dimensionless because CSEI has units of year^{-1}. In the locked monthly implementation, the nominal CSEI first became non-negative at month 211, corresponding to 17.5833 years and reported as 17.58 years. This is a monthly-grid onset estimate rather than a continuously interpolated crossing time.

To examine the limitation of the frozen-time interpretation, the variational system

$$\frac{d\Phi(t,\ t_0)}{dt} = J[x(t),\ t]\Phi(t,\ t_0), \qquad \Phi(t_0,\ t_0) = I \tag{15}$$

was integrated along the non-autonomous reference trajectory. Finite-time amplification was quantified as

$$G(t_0,\ \Delta) = \sigma_{\max}\left[\Phi(t_0 + \Delta,\ t_0)\right] \tag{16}$$

The equivalent logarithmic gain was calculated as

$$geq(t_0,\ \Delta) = \ln\left[G(t_0,\ \Delta)\right]/\Delta \tag{17}$$

where Δ is expressed in years.

Finite-time gains were evaluated for selected 3-, 6- and 12-month windows at representative pre-crossing and post-crossing start years. For the reported CSEI, the climate term in the frozen Jacobian was fixed at its annualised reference value C_J=1.0. In contrast, the finite-time variational analysis retained the actual month-dependent climate multiplier C_j along the non-autonomous reference trajectory. Singular values were calculated using the Euclidean norm of the native normalised state coordinates $[D, L, H]^T$. Because finite-time singular-value gains depend on coordinate scaling, the reported values are diagnostics of transient amplification within the adopted state representation rather than invariant physical-energy gains. The annualised climate value was used in the frozen-time CSEI to isolate the slow lifecycle feedback from purely seasonal sign oscillations. Month-dependent climate forcing remained active in state propagation, uncertainty analysis and the finite-time variational diagnostic.

Table 3. Locked reference state and energy-coupling parameters used throughout the analysis.

Symbol	Reference value	Unit/meaning
k_D	0.01382	year^{-1}; baseline deterioration
q_D	0.03911	year^{-1}; nonlinear deterioration acceleration
c_H	0.00400	year^{-1}; thermal-load feedback to D
k_L	0.00986	year^{-1}; baseline envelope-loss progression
c_D	0.02046	year^{-1}; deterioration-to-envelope coupling
c_{LH}	0.00139	year^{-1}; thermal-load feedback to L
u_1	1.3919	linear envelope-loss amplification
u_2	4.3504	quadratic envelope-loss amplification
τ	0.4585	year; thermal-load memory
x_0	[0.02, 0.02, 1.00]^T	Initial state vector [D_0, L_0, H_0]^T; dimensionless
COP_{rel}	1.0000	Dimensionless nominal relative coefficient of performance

The values in Table 3 constitute the locked reference parameterisation used for the controlled numerical and probabilistic analyses. They were not estimated from the Building Data Genome

Project 2 electricity meter. The empirical evidence in the present study directly supports only the electricity-observation layer. The lifecycle percentages, state trajectories and CSEI onset are therefore conditional reference-scenario outputs rather than empirical estimates for a general building stock. Application to a specific asset requires a temporally aligned, multi-source calibration dataset combining structural-response features (e.g., modal frequencies, strain or inspection-derived condition indices), envelope-condition measurements (e.g., airtightness, moisture, thermography or inferred heat-loss coefficients), and operational/BMS records (e.g., HVAC power, runtime and indoor–outdoor conditions). The observation mappings for D, L and H should first be calibrated, followed by regularised estimation of the deterioration and coupling coefficients and validation on a withheld monitoring period. Parameter dependence and model discrepancy should then be quantified from the asset-specific dataset before probabilistic forecasts are used for decision support.

Table 4. Active and inactive pathways in the three coupling configurations.

Configuration	D→L through c_D	L→H through u_1 and u_2	H→D through c_H	H→L through c_{LH}
Energy-Energy-Energy-decoupled	Active	Inactive	Inactive	Inactive
One-way coupling	Active	Active	Inactive	Inactive
Bidirectional coupling	Active	Active	Active	Active

The term energy-decoupled refers to separation of the structural–envelope subsystem from the thermal-load memory state, not to removal of all coupling between D and L (Table 4). In the energy-decoupled configuration, $u_1=u_2=c_H=c_{LH}=0$ while c_D remains active. In the one-way configuration, c_D, u_1 and u_2 are active while $c_H=c_{LH}=0$. The bidirectional configuration retains all pathways. Initial states, climate inputs, time integration and all other parameters are identical across the three configurations.

4. Bayesian updating and uncertainty

4.1. Observation and updating model

Quarterly observations combine a normalised structural-frequency proxy $y_f=\sqrt{1-D}+\varepsilon_f$, an envelope-loss observation y_L=L+ε_L, and a normalised thermal-load observation y_H=H+ε_H. Their observation standard deviations are 0.003, 0.008 and 0.020, respectively. In the controlled recovery experiment, D is interpreted specifically as a normalised effective stiffness-loss coordinate under an unchanged effective-mass assumption. The frequency relation is therefore an illustrative reduced-order observation function rather than a building-specific modal model.

Sequential importance-resampling particle filtering was used for state tracking under uncertain parameters (Särkkä 2013). The augmented particle vector was $\xi_k=[D_k, L_k, H_k, k_D, q_D, c_H, c_D, u_2]^T$. The remaining parameters k_L, c_{LH}, u_1 and τ were held at their reference values. All particles were initialised at the known initial state $[0.02, 0.02, 1.00]^T$, while the five parameter particles were drawn independently from lognormal priors with the biased means and coefficients of variation reported below. At each quarterly update, particles were propagated through the state and parameter transition models, weighted with the Gaussian observation likelihood, normalised, and systematically resampled only when the effective sample size fell below 50% of the 2,500-particle population. Posterior state means and 95% intervals were calculated from the normalised weighted particle population before resampling. Quarterly state-process standard deviations were 0.00015, 0.00020 and 0.00150 for D, L and H. Parameter particles followed a log-space random walk with standard deviation 0.00150 per update. The synthetic-observation and particle-filter seeds were

20260805 and 20260827. Parameter-particle trajectories represent propagated uncertainty and are distinct from the regularised point estimates reported separately.

A separate regularised parameter-recovery step was applied to k_D, c_D and u_2. This step produced regularised point estimates rather than a complete posterior parameter distribution. Particle-based state estimation and regularised parameter recovery are therefore reported separately. The biased prior means relative to the reference values were 0.88 for k_D, 0.85 for q_D, 0.90 for c_H, 0.90 for c_D and 0.82 for u_2. Corresponding prior coefficients of variation were 22%, 25%, 25%, 25% and 22%.

Regularised parameter recovery minimised the weighted observation-residual and prior-deviation objective:

$$\mathcal{L}(\theta) = \sum_{k=1}^{K} \left[y_k - h(x_k,\ \theta)\right]^T R^{-1} \left[y_k - h(x_k,\ \theta)\right] + \lambda\left(\theta - \theta_{prior}\right)^T W \left(\theta - \theta_{prior}\right) \tag{18}$$

Here $R = diag(0.003^2, 0.008^2, 0.020^2)$, $\lambda = 1.0$, and $W = diag[(0.22\ k_{D,prior})^{-2}$, $(0.25\ c_{D,prior})^{-2}$, $(0.22\ u_{2,prior})^{-2}]$. The three diagonal entries of W correspond to the inverse squared prior standard deviations of the recovered parameters k_D, c_D, and u_2, respectively. The optimisation variables were bounded to 0.5–1.5 times their reference values and initialised at the biased prior means. L-BFGS-B was used with a maximum of 2,000 iterations, function tolerance 10^{-12} and projected-gradient tolerance 10^{-8}. Each objective evaluation used the same monthly RK4 state integration and quarterly observation schedule.

For recovery experiment r and state $s \in \{D, L, H\}$, trajectory RMSE and pointwise interval coverage were defined as:

$$RMSE_s^{(r)} = \sqrt{\frac{1}{K}\sum_{k=1}^{K}\left(\hat{s}_k^{(r)} - s_k^{(r)}\right)^2} \tag{19}$$

$$Coverage_s = \frac{1}{100K}\sum_{r=1}^{100}\sum_{k=1}^{K} I\left[s_k^{(r)} \in C_{0.95,k}^{(r)}\right] \tag{20}$$

The reported state errors are the medians of RMSEs(r) across 100 experiments. Onset error was the predicted CSEI zero-crossing time minus the reference zero-crossing time; median absolute onset error and mean signed onset error were reported separately. All 100 controlled recovery trajectories crossed within the 25-year horizon, so no onset value was censored in this experiment. The repeated experiments were correctly specified inverse tests because the synthetic observations and estimator used the same state and observation model classes. They assess numerical and statistical recoverability under the prescribed sensor configuration, not robustness to deterioration-law, observation-function or structural model discrepancy.

4.2. Uncertainty propagation

All positive state-model parameters were sampled independently from lognormal distributions with the reference means reported in Table 3. Coefficients of variation were 15% for k_D and k_L; 20% for q_D, c_H, c_D and c_{LH}; 12% for u_1; 15% for u_2; and 10% for τ. A total of 5,000 parameter–climate realisations were generated using master seed 20260728. The same draws were used for all structural-coupling comparisons. Reported trajectory intervals are empirical 2.5–97.5 percentile intervals across realisations; uncertainty in ensemble means is reported separately through Monte Carlo standard errors and confidence intervals. Parameter dependence was not represented because no joint asset-calibration dataset was available. Independent lognormal marginals are therefore a scenario

assumption and may understate or overstate tail behaviour when deterioration and coupling coefficients are correlated.

The climate disturbance evolved continuously across the full 300-month horizon and was not reset at calendar-year boundaries:

$$\varepsilon_0 \sim \mathcal{N}\left(0,\ \sigma_\varepsilon^2\right), \qquad \varepsilon_j = \rho\varepsilon_{j-1} + \sigma_\varepsilon\sqrt{1-\rho^2}z_j, \qquad z_j \sim \mathcal{N}(0,\ 1) \tag{21}$$

Here ρ=0.65 and σ_ε=0.04, making 0.04 the stationary standard deviation and $\sigma_\varepsilon\sqrt{(1-\rho^2)}$ the innovation standard deviation. The initial deviation was drawn from the stationary distribution.

4.3. Nine-parameter global sensitivity analysis

The sensitivity analysis covered the nine uncertain positive state-model parameters listed in Table 3 and used the same independent lognormal marginals as the Monte Carlo analysis. It did not vary the baseline EUI, monthly load shares, HVAC share, grid-emission assumptions, initial states or model structure. Accordingly, “global” refers to the prescribed nine-dimensional state-parameter domain.

Jansen total-effect indices were estimated using a scrambled Sobol base sample of N=2,048 following Jansen (1999), Sobol (2001) and Saltelli et al. (2010). Bootstrap uncertainty was evaluated by resampling the 2,048 base-row indices with replacement while preserving the corresponding A, B and ABi row blocks. Total-effect indices were recalculated for 500 paired percentile-bootstrap resamples generated with seed 20260728, and the 2.5th and 97.5th percentiles defined the reported intervals.

The primary outputs were cumulative instability exposure J_{inst} and restricted time to onset T_R as defined in Equations (13–14). The binary crossing indicator was retained only as a secondary diagnostic because its near-unity crossing probability makes variance-based indices less stable. Only total-effect indices were estimated; the analysis does not claim a separate first-order interaction decomposition.

5. Results

5.1. Limiting cases and onset of instability

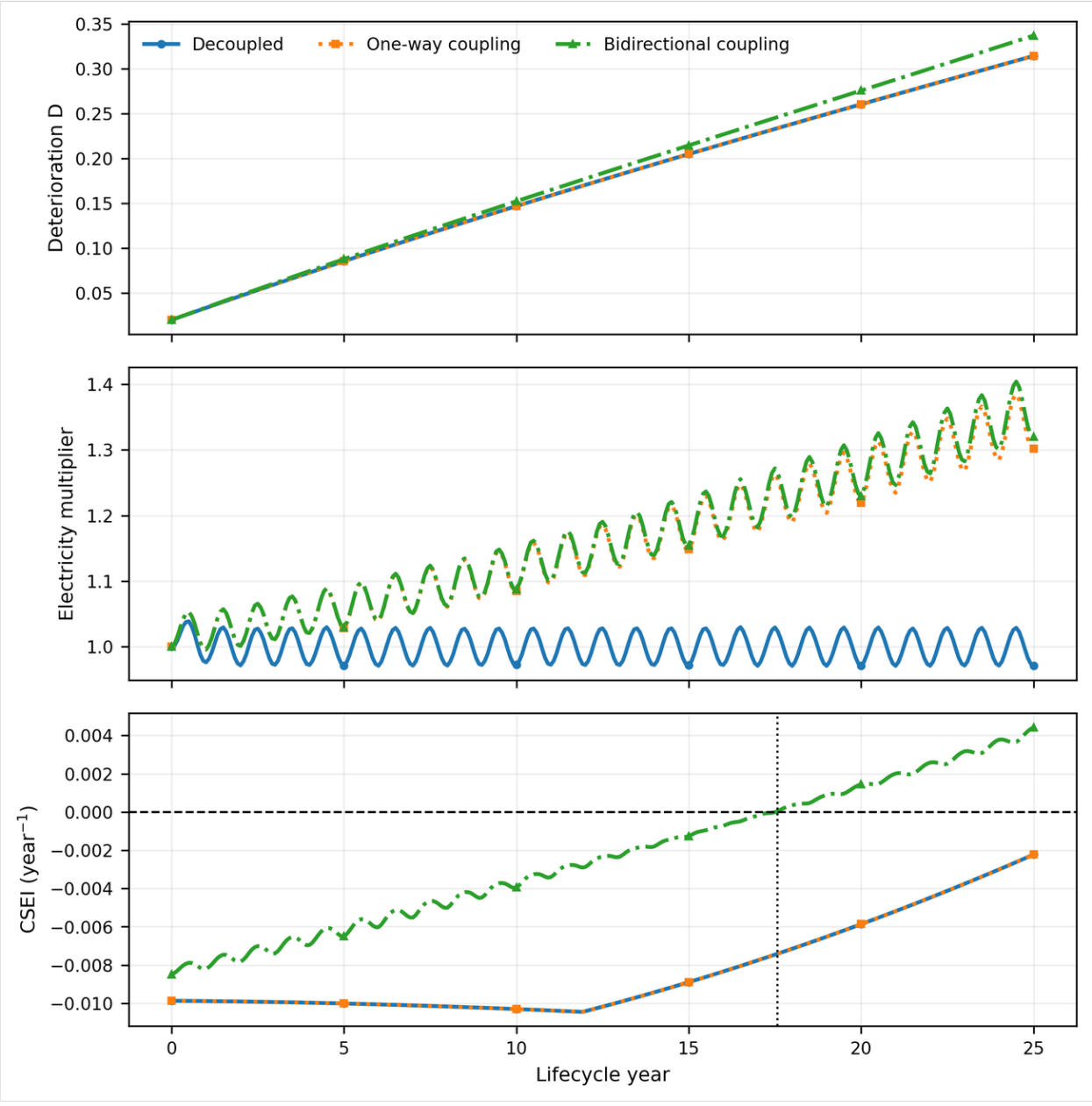

Figure 4. Twenty-five-year state, electricity-multiplier and CSEI trajectories for the energy-decoupled, one-way and bidirectionally coupled configurations. The energy-decoupled and one-way CSEI trajectories remain negative over the analysis horizon. The horizontal dashed line denotes CSEI=0, and the vertical line denotes the first non-negative bidirectional CSEI value on the monthly evaluation grid.

Table 5. Lifecycle outputs from the energy-decoupled, one-way and bidirectionally coupled reference configurations. Percentage changes reported in the text were calculated from unrounded outputs; displayed values are rounded for readability.

Metric	Energy-Energy-decoupled	One-way	Bidirectional
Final D	0.314	0.314	0.337
Final L	0.248	0.248	0.258
Final H	0.950	1.520	1.551
Lifecycle electricity (GWh)	27.48	31.90	32.06

Table 5. (continued)

Metric	Energy-Energy-decoupled	One-way	Bidirectional
Lifecycle carbon ($ktCO_2e$)	9.97	11.49	11.54
CSEI zero crossing	Not reached	Not reached	17.58 years
Cumulative instability exposure	0	0	0.01529

All percentage comparisons were calculated from unrounded simulation outputs. The one-way case separates the effect of a deteriorating envelope on electricity from the return feedback to deterioration (Figure 4 and Table 5). It raises lifecycle electricity from 27.48 to 31.90 GWh but leaves D unchanged. Activating the return path raises final D by 7.2% and produces a positive CSEI after 17.58 years. Relative to the Energy-Energy-decoupled model, lifecycle electricity rises by 16.7% and carbon by 15.8%. The smaller carbon percentage follows from the declining grid-factor scenario, which reduces the carbon weight of later energy amplification.

5.2. Probabilistic trajectories

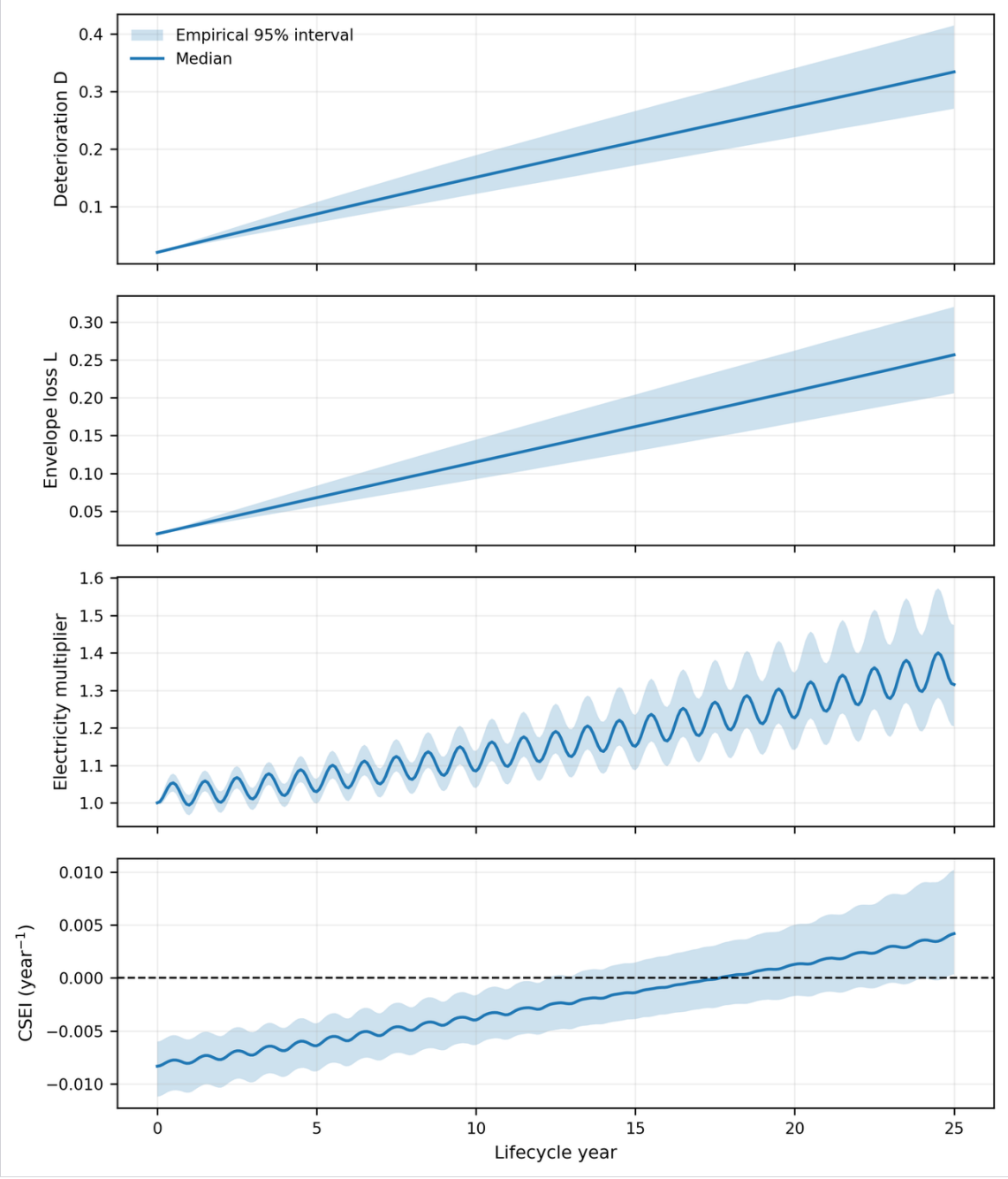

Figure 5. Median trajectories and empirical 2.5–97.5 percentile intervals for deterioration, envelope loss, whole-building electricity multiplier and CSEI across 5,000 parameter–climate realisations.

Table 6. Probabilistic summary statistics and 95% uncertainty/confidence intervals for lifecycle state, electricity, carbon and CSEI-related outputs across 5,000 parameter–climate realisations.

Output	Statistic	Estimate	95% uncertainty interval
Final D	Mean	0.337072	0.268455–0.414853
Final L	Mean	0.257619	0.205500–0.319348
Final H	Mean	1.551801	1.346542–1.826994
Lifecycle electricity	Mean	32.091415 GWh	30.675581–33.987535 GWh

Table 6. (continued)

Output	Statistic	Estimate	95% uncertainty interval
Lifecycle carbon	Mean	11.551830 $ktCO_2e$	11.068753–12.199780 $ktCO_2e$
Cumulative instability exposure	Mean	0.017581	0.000040–0.055059
Time to first non-negative CSEI	Median conditional on crossing	17.6667 years	12.2500–23.7500 years
Crossing by year 25	Proportion	4,918/5,000 = 98.36%	97.97–98.69%

Note: Intervals for continuous state, electricity, carbon and exposure outputs are empirical 2.5–97.5 percentiles across 5,000 parameter–climate realisations. The crossing-probability interval is an exact two-sided 95% Clopper–Pearson confidence interval. Onset summaries are conditional on crossing and are resolved on the monthly evaluation grid. The 82 non-crossing trajectories are right-censored at year 25 and assigned TR=25 only for the restricted-onset sensitivity output. Across 5,000 realisations, mean final D, L and H were 0.337072, 0.257619 and 1.551801. Mean lifecycle electricity and carbon were 32.091415 GWh and 11.551830 $ktCO_2e$. CSEI first became non-negative by year 25 in 4,918 of 5,000 realisations, corresponding to 98.36% with an exact two-sided 95% Clopper–Pearson interval of 97.97–98.69%. Conditional on crossing, the monthly-grid median onset was 17.67 years and the empirical 95% interval was 12.25–23.75 years. These are conditional scenario distributions rather than total predictive intervals for a real building.

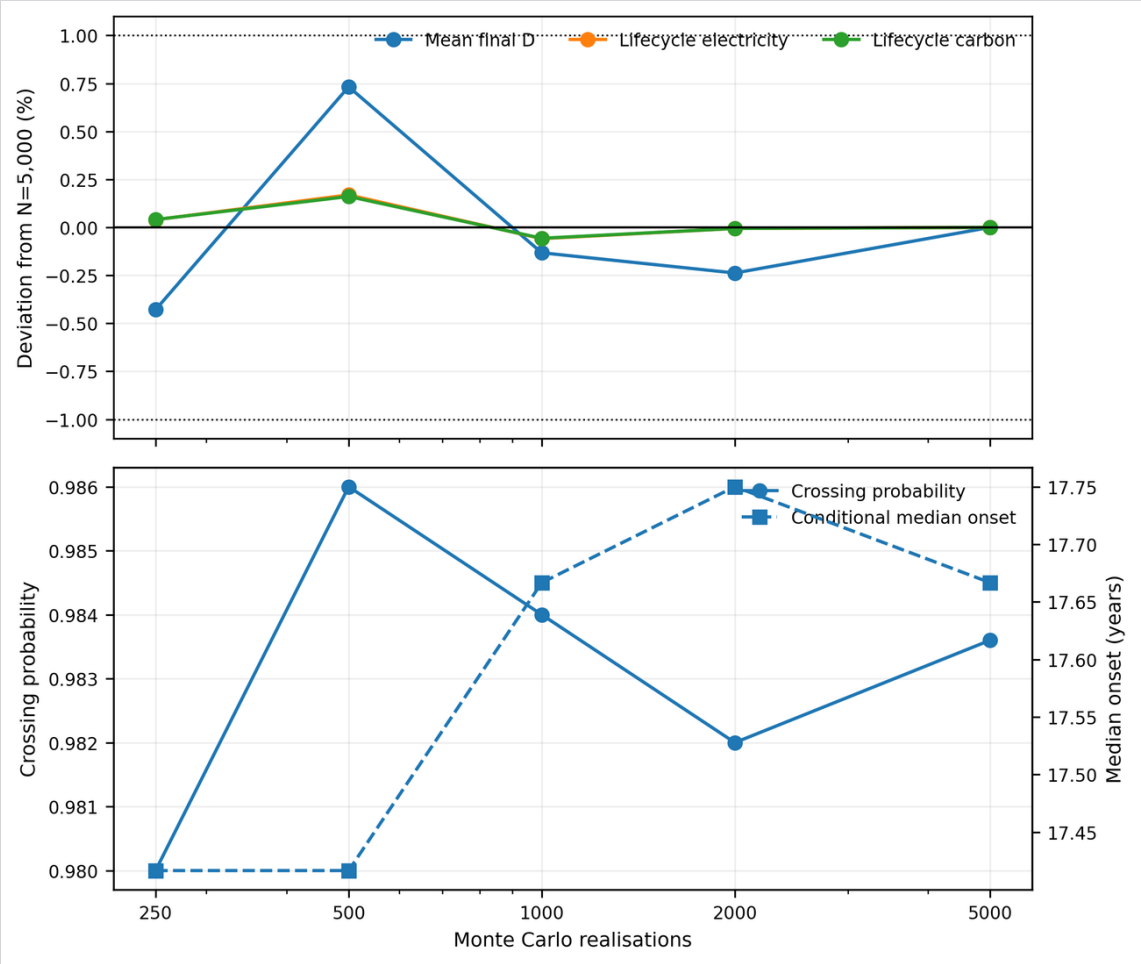

Figure 6. Monte Carlo convergence relative to the 5,000-realisation estimates for final deterioration, lifecycle electricity, lifecycle carbon, crossing probability and conditional median onset.

Prefix estimates from N=1,000 to N=5,000 remained close to the final 5,000-realisation results (Figure 6). At N=5,000, the Monte Carlo standard error was 0.000533 for mean final D, 0.004078 $ktCO_2e$ for mean lifecycle carbon and 0.001796 for crossing probability. The corresponding normal-approximation 95% confidence intervals were 0.336028–0.338117 for mean final D and 11.543838–11.559822 $ktCO_2e$ for mean lifecycle carbon (Figure 5 and Table 6). The exact two-sided 95% Clopper–Pearson interval for crossing probability was 0.9797–0.9869. Prefix convergence is presented as a numerical diagnostic and not as an independent uncertainty experiment.

5.3. Updating performance

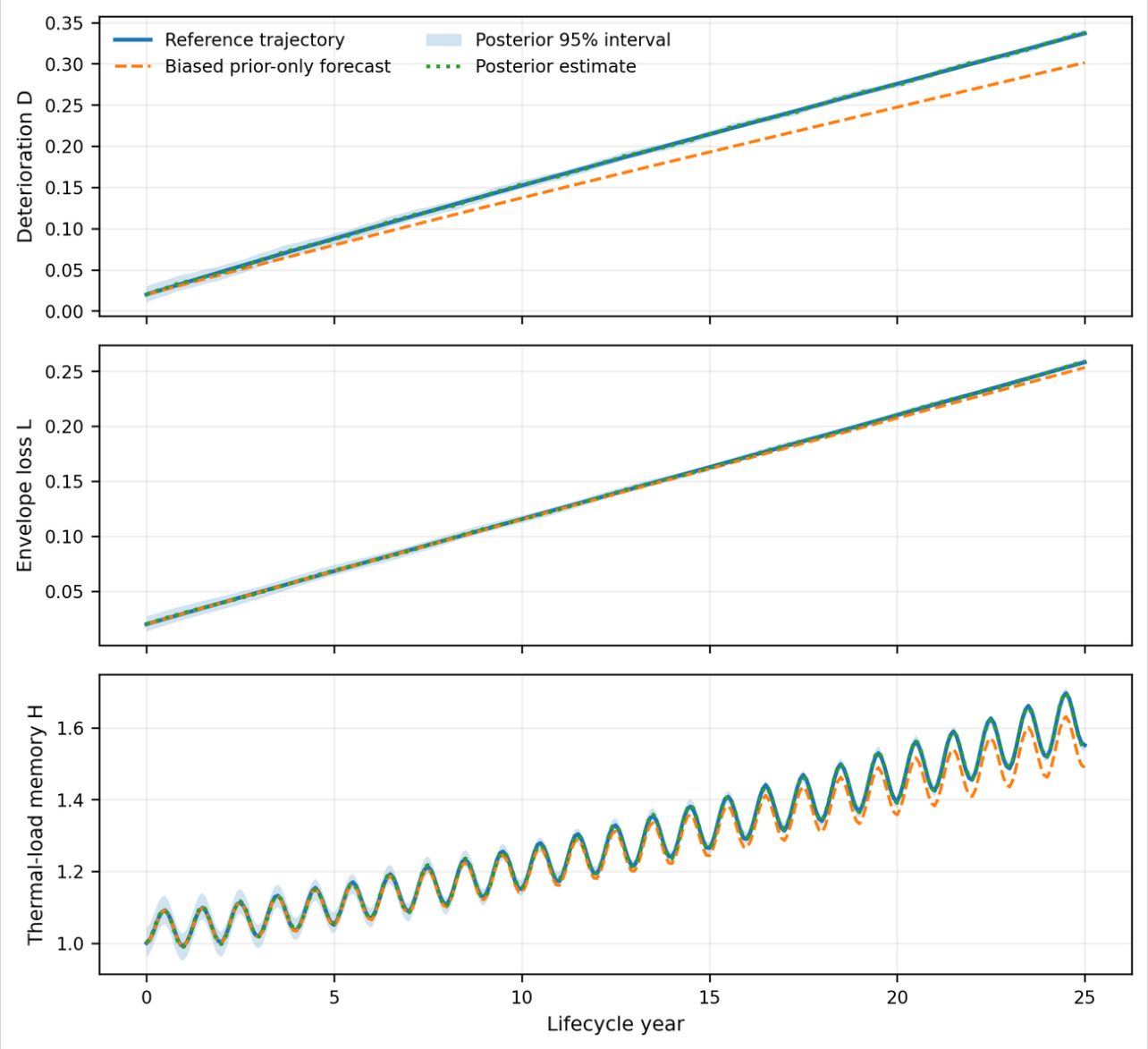

Figure 7. Reference trajectory, biased prior-only forecast, quarterly posterior state estimate and posterior 95% interval in the representative recovery experiment.

5.4. Panel A — Reference recovery experiment

Table 7. State-estimation and regularised parameter-recovery performance in the reference experiment and across 100 correctly specified synthetic recovery experiments

Metric	Biased prior-only forecast	Sequential particle-filter state estimate	Regularised parameter-calibrated trajectory	Interpretation
RMSE of D	0.02077	0.00184	Not applicable	91.2% lower after state assimilation
RMSE of L	0.00198	0.00108	Not applicable	45.3% lower after state assimilation
RMSE of H	0.02883	0.00741	Not applicable	74.3% lower after state assimilation
Reconstructed CSEI onset	21.83 years	Not reported separately	17.17 years	Reference monthly-grid onset: 17.58 years
k_D recovery deviation	Not applicable	Particle uncertainty only	+0.04%	Regularised point estimate
c_D recovery deviation	Not applicable	Particle uncertainty only	+5.24%	Regularised point estimate
u_2 recovery deviation	Not applicable	Particle uncertainty only	−1.20%	Regularised point estimate

5.5. Panel B — Performance across 100 correctly specified synthetic recovery experiments

Metric	Median / coverage
Posterior RMSE of D	0.00205
Posterior RMSE of L	0.00121
Posterior RMSE of H	0.00785
Median absolute onset error	0.56 years
Mean signed onset error	−0.11 years
95% interval coverage for D	94.0%
95% interval coverage for L	94.8%
95% interval coverage for H	95.2%

In the reference recovery experiment, the biased prior-only trajectory placed the CSEI transition 4.25 years later than the monthly-grid reference onset (Figure 7). Sequential particle filtering reduced state-tracking errors, while the separate regularised parameter-calibrated trajectory reduced the absolute onset-reconstruction error to 0.42 years (Table 7). Across 100 correctly specified synthetic recovery experiments, median state RMSEs remained low, the median absolute onset-reconstruction error was 0.56 years, and nominal 95% state intervals achieved 94.0–95.2% pointwise coverage. Because the full synthetic trajectories were used in these controlled inverse tests, these results represent retrospective recovery and reconstruction rather than prospective pre-onset forecasting. They do not establish identifiability under arbitrary sensor layouts or robustness to deterioration-law, observation-function or structural-model discrepancy.

5.6. CSEI verification and sensitivity

Table 8. Internal frozen-state consistency check for the CSEI implementation.

Lifecycle year	CSEI (year^{-1})	Growth rate from exp(JΔt) (year^{-1})	Five-year amplitude ratio
10	-0.003962	-0.003962	0.9804
20	0.001436	0.001436	1.0072
24	0.003773	0.003773	1.0190

The matrix-exponential calculation reproduces the spectral-abscissa rate of the same frozen Jacobian to numerical precision (Table 8). At year 10 the dominant frozen mode decays, whereas at years 20 and 24 it grows. This is an internal modal-consistency check; because both quantities derive from the same Jacobian, it is not an independent validation of the state model or a proof of global instability.

Table 9. Selected finite-time singular-value gains along the non-autonomous reference trajectory.

Start year	Window (months)	$\sigma_{max}(\Phi)$	Equivalent logarithmic gain (year^{-1})
10	3 months	1.5397	1.7263
10	6 months	2.0440	1.4299
10	12 months	2.2799	0.8241
17	3 months	1.7412	2.2183
17	12 months	2.7204	1.0008
20	3 months	1.8320	2.4215
20	12 months	2.9142	1.0696
24	12 months	3.1776	1.1561

The frozen-eigenmode calculation confirms the intended local interpretation of CSEI. The singular-value results additionally show that finite-time norm amplification may occur while CSEI remains negative because the system is time varying and non-normal (Table 9). The reported gains depend on the adopted normalised state coordinates and Euclidean norm; they are not invariant physical-energy amplification factors. H2 is therefore supported only as detection of a frozen-modal sign change, not as proof that every perturbation decays before that crossing.

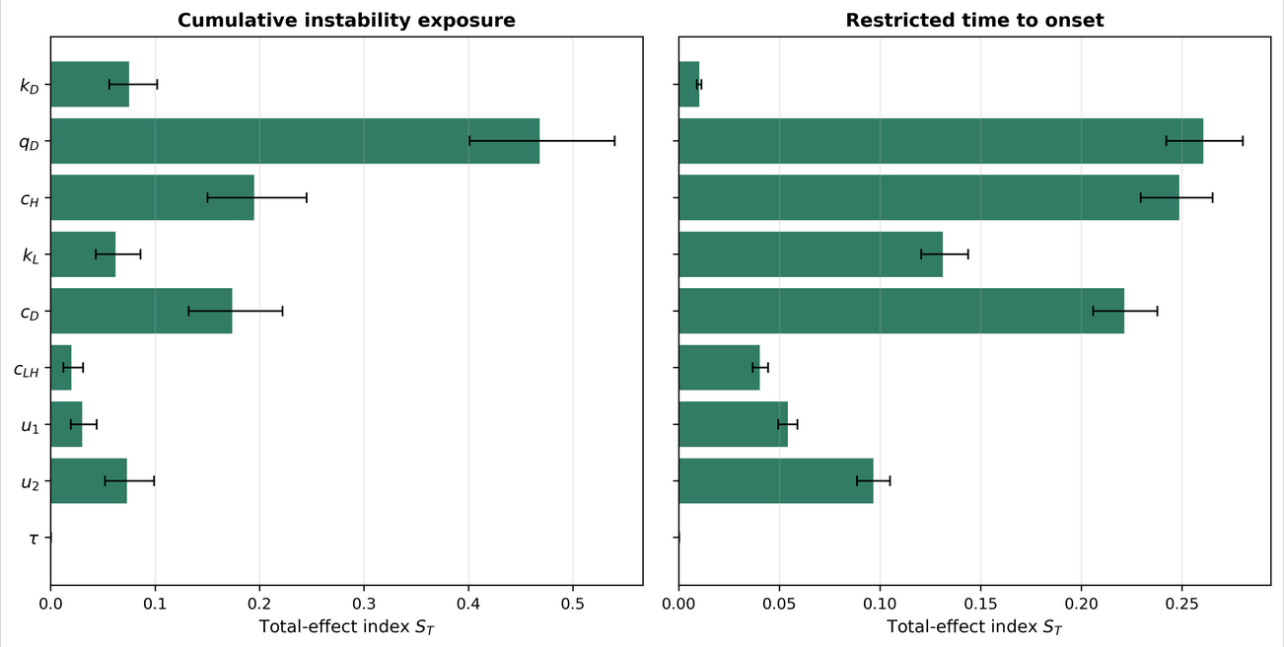

Figure 8. Jansen total-effect Sobol indices for cumulative instability exposure and restricted time to onset. Error bars show 95% bootstrap intervals for both outputs.

For cumulative instability exposure, q_D had the largest total effect, ST=0.4682 (95% CI: 0.4010–0.5400), followed by c_H, ST=0.1946 (0.1500–0.2450), and c_D, ST=0.1738 (0.1320–0.2220) (Figure 8 and Table 10). For restricted onset, the leading indices were q_D=0.2605 (0.2422–0.2801), c_H=0.2486 (0.2295–0.2652) and c_D=0.2213 (0.2058–0.2377). The remaining restricted-onset intervals were k_D 0.0089–0.0113, k_L 0.1204–0.1437, c_{LH} 0.0367–0.0444, u_1 0.0494–0.0590, u_2 0.0885–0.1049 and τ 0.00009–0.00024. H4 is therefore supported: uncertainty in nonlinear acceleration and the bidirectional operational feedback pathway dominates instability behaviour.

Table 10. Jansen total-effect indices for cumulative instability exposure and restricted time to onset.

Parameter	Exposure S_T	95% interval	Restricted-onset S_T	95% interval
k_D	0.0751	0.0561–0.1020	0.0102	0.0089–0.0113
q_D	0.4682	0.4010–0.5400	0.2605	0.2422–0.2801
c_H	0.1946	0.1500–0.2450	0.2486	0.2295–0.2652
k_L	0.0620	0.0430–0.0860	0.1311	0.1204–0.1437
c_D	0.1738	0.1320–0.2220	0.2213	0.2058–0.2377
c_{LH}	0.0198	0.0120–0.0310	0.0402	0.0367–0.0444
u_1	0.0300	0.0190–0.0440	0.0542	0.0494–0.0590
u_2	0.0729	0.0520–0.0990	0.0967	0.0885–0.1049
τ	0.0000	0.0000–0.0002	0.0002	0.00009–0.00024

6. Discussion

6.1. Evaluation of the hypotheses

H1 is supported within the locked reference scenario. Relative to the energy-decoupled configuration, bidirectional coupling increased lifecycle electricity by 16.7%, lifecycle carbon by 15.8% and final D by 7.2%. The one-way configuration showed that most of the electricity increase arose from the D-to-L-to-H pathway, whereas the additional increase in D required activation of the return H-to-D pathway.

H2 is supported only in its stated frozen-modal sense. On the monthly evaluation grid, the nominal CSEI first became non-negative at 17.58 years, when D, L and H were approximately 0.2462, 0.1872 and 1.4582. The matrix-exponential calculation reproduced the frozen spectral-abscissa rate. Finite-time singular-value analysis nevertheless showed that negative CSEI does not exclude transient norm amplification. CSEI must therefore be interpreted as a local modal-transition diagnostic rather than a complete global-stability measure.

H3 is supported for the correctly specified synthetic inverse tests. In the reference experiment, sequential assimilation reduced state RMSEs by 45.3–91.2%, while regularised parameter recovery reduced the absolute onset-reconstruction error from 4.25 to 0.42 years. Across 100 experiments, the median absolute onset-reconstruction error was 0.56 years and nominal 95% state intervals achieved 94.0–95.2% pointwise coverage. These results do not constitute prospective forecasting or external model-form validation.

H4 is supported within the nine-dimensional lognormal parameter domain. Nonlinear deterioration acceleration q_D was the dominant driver of cumulative exposure, while c_H and c_D demonstrated the importance of both directions of the structural–envelope–thermal feedback. The indices do not include uncertainty in the baseline EUI, HVAC share, initial states, grid-emission trajectory or model structure.

6.2. Validation achieved beyond equation verification

The evidence extends beyond reproduction of the state equations but remains deliberately hierarchical. The electricity-observation layer was evaluated one step ahead on a complete unseen calendar year. Numerical behaviour was examined through limiting cases, time-step refinement, frozen-modal consistency and finite-time diagnostics. State estimation and regularised recovery were examined through 100 correctly specified synthetic inverse experiments. Probabilistic outputs were supported by 5,000 realisations, Monte Carlo sampling-error estimates and bootstrap intervals for the nine-parameter total-effect indices. These steps establish empirical validity for the operational observation layer and internal numerical, statistical and inference consistency for the coupled workflow. They do not replace long-term field validation of structural and envelope deterioration.

6.3. Engineering and asset-management implications

The results indicate that structural condition, envelope performance, and HVAC operation should be treated as interacting components of a unified lifecycle-management system rather than as independent monitoring streams. In a practical implementation, the structural/support-condition state, (D), could be informed by calibrated modal features, strain measurements, or inspection-derived condition indices; the envelope-loss state, (L), by airtightness testing, façade moisture sensing, thermographic surveys, or inferred heat-loss coefficients; and the thermal-load memory state, (H), by plant power demand, HVAC runtime, and indoor–outdoor thermal gradients. Joint assimilation of these observations at regular intervals would allow the posterior state estimates, CSEI distribution, and projected onset time to be updated as new evidence becomes available.

Operational deployment would begin with an asset-specific baseline survey and a data-integration layer linking structural-monitoring systems, façade and envelope inspections, utility metering, and building-automation-system records. These heterogeneous observations would be mapped to the corresponding (D), (L), and (H) state variables and assimilated through the updating framework. The resulting posterior states would then propagate into the CSEI and lifecycle energy–carbon modules, allowing updated diagnostics and projections to be communicated through a facility- or asset-management platform. Such an implementation could support risk-informed structural inspections, prioritisation of façade and envelope remediation, targeted HVAC maintenance, and periodic model recalibration. Before operational decision support, however, the framework would require asset-specific parameter calibration, prospective validation of state-recovery and forecast performance, and explicit assessment of model discrepancy using co-located field observations.

The practical value of the framework therefore lies primarily in the evolution of the joint state rather than in any single reference onset year. A building may exhibit moderate structural/support deterioration, progressive envelope loss, and persistent thermal loading without any individual variable exceeding a conventional alarm threshold, while their coupled dynamics simultaneously move the system toward a non-negative CSEI. This finding supports coordinated assessment of structural, façade, and mechanical systems and cautions against lifecycle decisions based solely on isolated damage indices, fixed condition thresholds, or annual energy-use indicators.

The implications also extend directly to lifecycle energy and carbon management. Within the locked reference scenario, bidirectional coupling increased lifecycle electricity consumption by 16.7% relative to the energy-decoupled configuration. This result illustrates why a commissioning-year energy model should not automatically be extrapolated across the full-service life when envelope condition, HVAC operation, and deterioration-related feedback can evolve materially over time. Degradation-aware operational projections, periodically updated with measured asset data, can therefore provide a more defensible basis for long-term maintenance planning, energy management, and carbon-performance assessment.

6.4. Generalisation assumptions and limitations

Framework generalisation and numerical generalisation must be distinguished. The architecture is transferable, but the numerical parameterisation is not. For a new asset, the state definitions and observation functions should be adapted to the structural system and envelope type, while climate forcing, occupancy schedules, HVAC topology, baseline EUI and uncertainty distributions should be re-estimated from local data. Application to reinforced-concrete, steel, timber, masonry or hybrid buildings and to other climates therefore requires asset-specific recalibration rather than direct reuse of the 17.58-year onset or the reported lifecycle percentages.

The reported numerical results are conditional on a controlled reference parameterisation rather than an asset-calibrated deterioration model. Empirical validation is limited to one-step-ahead electricity observations from one office meter. The structural and envelope states, observation mappings and feedback coefficients were evaluated through correctly specified synthetic recovery experiments and therefore do not represent external model-form validation.

The uncertainty intervals exclude uncertainty in the baseline EUI, HVAC share, monthly load profile, grid-emission trajectory, initial states, activation-function form, parameter dependence and model structure. The independent lognormal assumption may understate or overstate tail behaviour when coefficients are correlated.

The nominal 17.58-year onset is the first non-negative CSEI value on a monthly evaluation grid and applies only to the locked reference scenario. CSEI is the spectral abscissa of a frozen local Jacobian; it is not a measure of structural safety, global nonlinear stability, collapse probability, occupant comfort or code compliance. Prospective deployment requires co-located structural, envelope and operational observations, asset-specific parameter calibration, pre-onset forecast validation, explicit model-discrepancy treatment and independent field evaluation.

7. Conclusions

This study developed an energy-data-anchored probabilistic digital-twin framework for long-horizon structural/support-condition, envelope and thermal-load interaction. The electricity-observation model retained its one-step-ahead performance on an independent 2017 calendar year, achieving R^2=0.933, CV(RMSE)=6.65% and NMBE=0.029%.

Within the locked 25-year reference scenario, bidirectional coupling increased lifecycle electricity and carbon by 16.7% and 15.8% relative to the energy-decoupled configuration. CSEI first became non-negative at month 211, corresponding to 17.58 years on the monthly evaluation grid. Across 5,000 parameter–climate realisations, mean lifecycle electricity and carbon were 32.091 GWh and 11.552

$ktCO_2e$, and 98.36% of trajectories crossed by year 25, with a conditional monthly-grid median onset of 17.67 years.

Sequential particle filtering reduced state-tracking errors, while separate regularised parameter recovery improved retrospective reconstruction of the CSEI onset. Across 100 correctly specified synthetic inverse tests, state-interval coverage remained close to the nominal 95% level. Nine-parameter total-effect analysis identified nonlinear deterioration acceleration and the bidirectional feedback coefficients as the principal drivers of the two instability outputs. For building owners and facility managers, the practical implication is that structural condition, envelope performance and HVAC operation should be treated as a jointly updated asset-management problem rather than as independent monitoring streams. The framework can support risk-informed inspection timing, façade and HVAC maintenance prioritisation, and revision of long-term energy and carbon forecasts as new observations become available. In the reference scenario, the difference between the energy-decoupled and bidirectionally coupled cases—16.7% in lifecycle electricity and 15.8% in lifecycle carbon—quantifies the potential consequence of neglecting deterioration–energy feedback within the stated modelling assumptions.

The transferable contribution is the integration of an empirical electricity-observation layer, a coupled lifecycle state model, sequential updating, conditional uncertainty propagation and a deliberately limited local modal diagnostic. The numerical percentages and onset times are reference-scenario outputs. They should not be interpreted as field-validated deterioration predictions, global-stability results or structural-safety criteria.

Appendix A. Reproducibility settings

Monthly state integration used fixed-step classical fourth-order Runge–Kutta with one primary step per month. Time-step verification used 2, 4 and 8 substeps per month. The lifecycle horizon was 25 years. The nominal onset was defined as the first non-negative CSEI value on the corresponding evaluation grid; no interpolation between grid points was applied. Parameter–climate uncertainty used 5,000 realisations and master seed 20260728. Particle filtering used 2,500 particles, systematic resampling at ESS<0.50N, synthetic-observation seed 20260805 and particle-filter seed 20260827. The nine-parameter Sobol analysis used a scrambled base sample of 2,048 and 500 paired bootstrap resamples. Numerical diagnostic bounds were $0 \leq D,L \leq 0.99$ and $0.05 \leq H \leq 5.0$; no reported reference or uncertainty trajectory reached these bounds.

Table A1. Empirical monthly whole-building electricity shares.

Month	Electricity share
January	0.081000
February	0.076000
March	0.078000
April	0.079000
May	0.082000
June	0.086000
July	0.093000
August	0.096000
September	0.088000
October	0.083000
November	0.079000
December	0.079000
Sum	**1.000000**

Table A2. Reference state-model parameters and uncertainty distributions.

Parameter	Mean	CV	Distribution
k_D	0.01382 year^{-1}	15%	Lognormal
q_D	0.03911 year^{-1}	20%	Lognormal
c_H	0.00400 year^{-1}	20%	Lognormal
k_L	0.00986 year^{-1}	15%	Lognormal
c_D	0.02046 year^{-1}	20%	Lognormal
c_{LH}	0.00139 year^{-1}	20%	Lognormal
u_1	1.3919	12%	Lognormal
u_2	4.3504	15%	Lognormal
τ	0.4585 year	10%	Lognormal

Table A3. State-estimation and parameter-recovery settings.

Setting	Value
Assimilation frequency	Quarterly
Particles	2,500
Resampling	Systematic at ESS<0.50N
Observation SD: y_f, y_L, y_H	0.003, 0.008, 0.020
State-process SD: D, L, H	0.00015, 0.00020, 0.00150
Parameter log-random-walk SD	0.00150 per update
Prior mean/reference: k_D, q_D, c_H, c_D, u_2	0.88, 0.85, 0.90, 0.90, 0.82
Prior CV	22%, 25%, 25%, 25%, 22%
Synthetic-observation seed	20260805
Particle-filter seed	20260827
Recovery repetitions	100
Initial state-particle distribution	Deterministic at D=0.02, L=0.02 and H=1.00
Parameter-prior distribution	Independent lognormal priors with biased means and CVs reported above
Augmented particle vector	$[D, L, H, k_D, q_D, c_H, c_D, u_2]^T$
Parameters held fixed	k_L, c_{LH}, u_1 and τ
Update order	Propagate; likelihood weight; normalise; compute summaries; resample if ESS<0.50N
Posterior summaries	Weighted mean and weighted 2.5–97.5% quantiles before resampling

Table A4. Numerical integration, uncertainty and sensitivity settings.

Setting	Value
Lifecycle horizon	25 years
Primary integration	Monthly fixed-step RK4
Time-step verification	1, 2, 4 and 8 substeps per month
Monte Carlo realisations	5,000
Monte Carlo seed	20260728
Sobol base sample	2,048
Sobol bootstrap resamples	500
Diagnostic state bounds	$0 \le D, L \le 0.99; 0.05 \le H \le 5.0$
Observation-model regularisation	α=10 fixed a priori; native-unit predictors; no test-year tuning
Sobol bootstrap method	Paired base-row percentile bootstrap preserving A, B and ABi blocks

Table A4. (continued)

Setting	Value
Sobol bootstrap seed	20260728

Table A5. Time-step convergence of the nominal reference trajectory.

Substeps/month	Step (year)	Final D	Final L	Final H	CSEI onset (year)
1	0.083333	0.33693931	0.25817326	1.55157790	17.5833
2	0.041667	0.33693930	0.25817325	1.55157717	17.5417
4	0.020833	0.33693930	0.25817325	1.55157712	17.5208
8	0.010417	0.33693930	0.25817325	1.55157712	17.5208

State endpoints were invariant to the reported precision. The first non-negative CSEI value occurred at 17.5833 years with one substep per month and at 17.5208 years with four and eight substeps per month. The difference of 0.0625 years is approximately 0.75 months and reflects the discrete grid definition of onset. All principal reported analyses use the locked monthly grid; the onset is therefore reported as 17.58 years with an explicit one-month temporal resolution.

Table A6. Principal symbols and definitions.

Symbol	Definition	Unit
D	Structural/support-condition loss state	Dimensionless
L	Envelope thermal and leakage-loss state	Dimensionless
H	Thermal-load memory state	Dimensionless
C_j	Month-specific climate multiplier	Dimensionless
ε_j	Stationary AR(1) climate disturbance	Dimensionless
COP_{rel}	Nominal relative coefficient of performance	Dimensionless
E_0	Initial annual whole-building electricity	kWh $year^{-1}$
w_q	Empirical monthly electricity share	Dimensionless
f_{HVAC}	HVAC fraction of baseline whole-building electricity	Fraction
EF_j	Grid-emission factor in month j	$kgCO_2e\ kWh^{-1}$
J	Frozen local state Jacobian	$year^{-1}$
CSEI	Spectral abscissa of J	$year^{-1}$
T×	First non-negative CSEI time	year
T_R	Restricted time to onset	year
J_{inst}	Cumulative positive-CSEI exposure	Dimensionless
Φ	Variational state-transition matrix	Dimensionless
G	Maximum finite-time singular-value gain	Dimensionless

Declarations

Author contributions. Seyed Reza Samaei: Conceptualisation, methodology, software, formal analysis, investigation, data curation, validation, visualisation, writing—original draft, writing—review and editing, and project administration. Assed Naked Haddad: Methodology, validation, supervision, and writing—review and editing. James Riffat: Conceptualisation, methodology, validation, supervision, and writing—review and editing. All authors reviewed and approved the final manuscript.

Funding. This research received no specific grant from any funding agency in the public, commercial, or not-for-profit sectors. The work was completed using the authors' existing academic and computational resources.

Conflicts of interest. The authors declare that they have no competing financial or non-financial interests that could have influenced the research, analysis, interpretation, or reporting of the findings presented in this manuscript.

Data availability. The public meter, building metadata and weather records used for the empirical electricity analysis are available through the Building Data Genome Project 2 associated with Miller et al. (2020), DOI: 10.1038/s41597-020-00712-x. Appendix A reports the monthly load shares, state-model parameters, Bayesian settings, uncertainty distributions, random-number seeds and numerical convergence settings required to interpret the reported analysis. The processed inputs, numerical implementation, unrounded outputs and figure-generation scripts are available from the corresponding author upon reasonable request.

Ethics. This study used publicly available, non-personal building electricity, metadata and weather records from the Building Data Genome Project 2, together with synthetic structural–envelope trajectories generated for controlled recovery experiments. It involved no human participants, animals, biological materials, sensitive personal data or identifiable individuals. Ethics approval and informed consent were therefore not required.

Editorial independence. One or more authors of this paper serve as editors of this journal. To ensure editorial independence, these authors were fully recused from the handling of this manuscript. They took no part in the selection of reviewers, the peer-review process, or the editorial decision, which were managed independently by another editor with no involvement in the work.

References

Andrés Arcones, Daniel; Weiser, Martin; Koutsourelakis, Phaedon-Stelios; Unger, Jörg F. (2024) 'Model Bias Identification for Bayesian Calibration of Stochastic Digital Twins of Bridges', *Applied Stochastic Models in Business and Industry*, 41(3). Available at: https://doi.org/10.1002/asmb.2897

ASHRAE (2023) *ASHRAE Guideline 14-2023: Measurement of Energy, Demand, and Water Savings*. Atlanta, GA: American Society of Heating, Refrigerating and Air-Conditioning Engineers.

Boje, Calin; Guerriero, Annie; Kubicki, Sylvain; Rezgui, Yacine (2020) 'Towards a semantic Construction Digital Twin: Directions for future research', *Automation in Construction*, 114, pp. 103179. Available at: https://doi.org/10.1016/j.autcon.2020.103179

Deng, Min; Menassa, Carol C.; Kamat, Vineet R. (2021) 'From BIM to digital twins: a systematic review of the evolution of intelligent building representations in the AEC-FM industry', *Journal of Information Technology in Construction*, 26, pp. 58-83. Available at: https://doi.org/10.36680/j.itcon.2021.005

Hwang, Jaemin; Kim, Jiwon; Yoon, Sungmin (2025) 'DT-BEMS: Digital twin-enabled building energy management system for information fusion and energy efficiency', *Energy*, 326, pp. 136162. Available at: https://doi.org/10.1016/j.energy.2025.136162

Jansen, Michiel J.W. (1999) 'Analysis of variance designs for model output', *Computer Physics Communications*, 117(1-2), pp. 35-43. Available at: https://doi.org/10.1016/s0010-4655(98)00154-4

Kapteyn, Michael G.; Pretorius, Jacob V. R.; Willcox, Karen E. (2021) 'A probabilistic graphical model foundation for enabling predictive digital twins at scale', *Nature Computational Science*, 1(5), pp. 337-347. Available at: https://doi.org/10.1038/s43588-021-00069-0

Madni, Azad M.; Madni, Carla C.; Lucero, Scott D. (2019) 'Leveraging Digital Twin Technology in Model-Based Systems Engineering', *Systems*, 7(1), pp. 7. Available at: https://doi.org/10.3390/systems7010007

Miller, Clayton; Kathirgamanathan, Anjukan; Picchetti, Bianca; Arjunan, Pandarasamy; Park, June Young; Nagy, Zoltan; Raftery, Paul; Hobson, Brodie W.; Shi, Zixiao; Meggers, Forrest (2020) 'The Building Data Genome Project 2, energy meter data from the ASHRAE Great Energy Predictor III competition', *Scientific Data*, 7(1). Available at: https://doi.org/10.1038/s41597-020-00712-x

Oh, Ju-Hong; Sfarra, Stefano; Kim, Eui-Jong (2024) 'Hybrid modeling based on integrating simulation and operational data to improve indoor air temperature predictions, a controlled variable in digital twin models', *Energy and Buildings*, 324, pp. 114898. Available at: https://doi.org/10.1016/j.enbuild.2024.114898

Rasheed, Adil; San, Omer; Kvamsdal, Trond (2020) 'Digital Twin: Values, Challenges and Enablers From a Modeling Perspective', *IEEE Access*, 8, pp. 21980-22012. Available at: https://doi.org/10.1109/ACCESS.2020.2970143

Saltelli, Andrea; Annoni, Paola; Azzini, Ivano; Campolongo, Francesca; Ratto, Marco; Tarantola, Stefano (2010) 'Variance based sensitivity analysis of model output. Design and estimator for the total sensitivity index', *Computer Physics Communications*, 181(2), pp. 259-270. Available at: https://doi.org/10.1016/j.cpc.2009.09.018

Samaei, Seyed Reza; Riffat, James (2026) 'From Optimization to Stability Preservation: A Self-Healing, Action-Bearing Digital Twin for Climate-Stressed Building Energy Systems', *Green Technology & Innovation*, 2, pp. 150-177. Available at: https://doi.org/10.65582/gti.2026.008

Särkkä, Simo (2013) *Bayesian Filtering and Smoothing*. Cambridge University Press. Available at: https://doi.org/10.1017/CBO9781139344203

Sobol, I M (2001) 'Global sensitivity indices for nonlinear mathematical models and their Monte Carlo estimates', *Mathematics and Computers in Simulation*, 55(1–3), pp. 271–280. Available at: https://doi.org/10.1016/S0378-4754(00)00270-6

Sun, Zhiyan; Jayasinghe, Sanduni; Sidiq, Amir; Shahrivar, Farham; Mahmoodian, Mojtaba; Setunge, Sujeeva (2025) 'Approach Towards the Development of Digital Twin for Structural Health Monitoring of Civil Infrastructure: A Comprehensive Review', *Sensors*, 25(1), pp. 59. Available at: https://doi.org/10.3390/s25010059

Taki, Ahmad; Zakharanka, Anastasiya (2023) 'The Impact of Degradation on a Building's Energy Performance in Hot-Humid Climates', *Sustainability*, 15(2), pp. 1145. Available at: https://doi.org/10.3390/su15021145

Torzoni, Matteo; Manzoni, Andrea; Mariani, Stefano (2025) 'Enhancing Bayesian model updating in structural health monitoring via learnable mappings', *Engineering with Computers*, 41(6), pp. 4953-4975. Available at: https://doi.org/10.1007/s00366-025-02224-x

Wright, Louise; Davidson, Stuart (2020) 'How to tell the difference between a model and a digital twin', *Advanced Modeling and Simulation in Engineering Sciences*, 7(1). Available at: https://doi.org/10.1186/s40323-020-00147-4

HOW TO CITE THIS ARTICLE

Samaei, S. R., Naked Haddad, A. and Riffat, J. (2026). An Energy-Data-Anchored Probabilistic Digital-Twin Framework for Coupled Structural–Envelope Degradation and Local Energy-Demand Amplification in Low-Carbon Buildings. Green Technology & Innovation, 2, 410-436. https://doi.org/10.65582/gti.2026.018

COPYRIGHT AND LICENCE

© 2026 The Author(s). This is an open access article distributed under the terms of the Creative Commons Attribution (CC BY 4.0) licence, which permits unrestricted use, distribution and reproduction in any medium, provided the original work is properly cited.